AGU PUBLICATIONS

JGR

Journal of Geophysical Research: Atmospheres

RESEARCH ARTICLE
10.1002/2016JD025458

Key Points:
- Molecular dynamics (MD) reveals unsuspected properties of ice-vapor interfaces over a cycle of ice layer growth
- A new continuum model, based on insights from MD, complements existing theories of ice growth from vapor
- Robustness of faceted ice growth from vapor is traced to an underlying mathematical structure, a stable limit cycle

Supporting Information:
- Figure S1
- Movie S1
- Movie S2

Correspondence to:
S. Neshyba,
nesh@pugetsound.edu

Citation:
Neshyba, S., J. Adams, K. Reed, P. M. Rowe, and I. Gladich (2016), A quasi-liquid mediated continuum model of faceted ice dynamics, *J. Geophys. Res. Atmos.*, *121*, 14,035–14,055, doi:10.1002/2016JD025458.

Received 3 JUN 2016
Accepted 4 NOV 2016
Accepted article online 7 NOV 2016
Published online 10 DEC 2016

A quasi-liquid mediated continuum model of faceted ice dynamics

Steven Neshyba[1], Jonathan Adams[1], Kelsey Reed[1], Penny M. Rowe[2,3], and Ivan Gladich[4]

[1]Department of Chemistry, University of Puget Sound, Tacoma, Washington, USA, [2]Departamento de Fisica, Universidad de Santiago de Chile, Santiago, Chile, [3]NorthWest Research Associates, Redmond, Washington, USA, [4]Qatar Environment and Energy Research Institute, Hamad bin Kalifa University, Doha, Qatar

Abstract We present a quasi-liquid mediated continuum model for ice growth consisting of partial differential equations informed by molecular dynamics simulations. The main insight from molecular dynamics is the appearance of periodic variations in the equilibrium vapor pressure and quasi-liquid thickness of the ice/vapor interface. These variations are incorporated in the continuum model as subgrid scale microsurfaces. We show that persistent faceted ice growth in the presence of inhomogeneities in the ambient vapor field is due to a spontaneous narrowing of terraces at facet corners, which compensates for higher ambient water vapor density via feedback between surface supersaturation and quasi-liquid thickness. We argue that this emergent behavior has the mathematical structure of a stable limit cycle and characterize its robustness in terms of ranges of parameters that support it. Because the model is relevant in the high-surface-coverage regime, it serves as a useful complement to the Burton-Cabrera-Frank framework. Quantitative aspects and limitations of the model are also discussed.

1. Introduction

Cirrus clouds play an important role in the Earth's climate by absorbing and reflecting infrared and solar radiation [*Stephens et al.*, 1990; *Lynch*, 2002]. Those radiative properties, in turn, depend on the shape and surface morphology of ice crystals as they grow and sublimate [*Yang and Liou*, 1998; *Fu and Liou*, 2008; *Baran*, 2009, 2015; *Guignard et al.*, 2012; *Schnaiter et al.*, 2016]. While considerable efforts have been directed at understanding vapor-deposited ice crystal growth and sublimation at the atomistic and mesoscopic (micrometer) scales separately, a comprehensive theory that incorporates both scales has received much less attention. A theory of faceted ice growth and sublimation that bridges these scales, with transparent connections to relevant underlying atomistic processes, would allow us to better exploit our understanding at both scales and bring us closer to a predictive theory of atmospherically relevant ice crystal dynamics and shape.

It has long been recognized that isolated and defect-free ice crystals grown from the vapor do so by steps that originate at facet corners and propagate across an ice surface [*Hallett*, 1961; *Hobbs and Scott*, 1965a, 1965b; *Hobbs*, 2010]. Steps originate preferentially at facet corners because the concentration of water vapor above a growing ice facet is typically inhomogeneous, being greater at corners than over facet centers. While the inhomogeneity may be slight (water vapor moves through air much faster than surface-adsorbed water molecules move across ice surfaces), even a small excess would build up over time and result in hollowed or dendritic forms, all else equal. But faceted growth implies that all parts of a facet grow at the same rate. Indeed, the ubiquity of faceted ice in the natural atmosphere and laboratory conditions suggests that faceted growth is rather robust to deposition inhomogeneity.

Understanding the robustness of faceted ice growth therefore depends on a clear understanding of how excess water vapor deposited at the ice/vapor interface is converted to ice. This interface has a complex structure at atmospherically relevant temperatures, with a mobile quasi-liquid layer (QLL) transitioning to a more fixed ice-like lattice underneath [see, e.g., *Bartels-Rausch et al.*, 2012, 2014]. One way of characterizing the process of vapor deposition is through a quantity called a "condensation coefficient" or an "accommodation coefficient." Prior molecular dynamics (MD) [*Neshyba et al.*, 2009] and experimental [*Batista et al.*, 2005] studies have shown that the *surface accommodation coefficient* at the ice/vapor interface, defined on a picosecond time scale, is close to 1, but on the other hand, abundant experimental evidence shows that the *bulk accommodation coefficient*, defined on a much longer time scale, can be much smaller [*Magee et al.*, 2006; *Pratte et al.*, 2006; *Bartels-Rausch et al.*, 2012]. These observations suggest that control of bulk accommodation

lies not at the interface between the QLL and vapor but at the ice-like/quasi-liquid interface. Indeed, a two-stage kinetic scheme embodying these ideas has been demonstrated to successfully account for accommodation measurements across a wide range of temperatures [*Kong*, 2014; *Kong et al.*, 2014]. Bolstering this view is evidence that the development and propagation of steps is facet-specific; i.e., they are processes that are sensitive to the symmetry of the underlying facet [*Libbrecht*, 2003a, 2003b, 2005; *Libbrecht and Rickerby*, 2013]; this implies microscopic influence over those processes. Considerable progress in understanding those microscopic processes has been made in recent decades, thanks to increasingly sophisticated molecular dynamics (MD) models of water and a variety of experimental approaches [*Nada and van der Eerden*, 2003; *Sadtchenko and Ewing*, 2003; *Bailey and Hallett*, 2004, 2009; *Sadtchenko et al.*, 2004; *Abascal and Vega*, 2005; *Pi et al.*, 2009; *Sazaki et al.*, 2010; *Vega et al.*, 2011].

Despite these advances, however, a missing connection is a coarse-grained, mesoscopic theory capable of translating the above microscopic properties into mesoscopic ones (including the robustness of uniform growth). Here we attempt to fill this gap by means of a reaction-diffusion system of partial differential equations with dynamic vapor/quasi-liquid/ice partitioning. The quasi-liquid layer is modeled as a surface density, or equivalent thickness; hence, it is a *continuum* model. Each grid point of the model spans approximately the area of a single MD simulation, and subgrid processes are parameterized based on results and insights derived from MD simulations. The formalism is similar to that of the classical Burton, Cabrera, and Frank (BCF) framework in its view of crystal growth occurring on a staircase structure of steps and terraces, upon which adatoms are represented as a surface density that obeys a diffusion equation [*Burton and Cabrera*, 1949; *Cabrera and Burton*, 1949; *Burton et al.*, 1951; *Myers-Beaghton and Vvedensky*, 1991]. It is distinct, however, in that BCF theory is based on an assumption that adsorbed molecules move by hopping between adjacent lattice sites and is valid in a low surface-density regime (in the same way that the ideal gas theory is valid in the limit of low gas density) [*Patrone*, 2013; *Patrone et al.*, 2014], whereas the present formalism occupies the opposite extreme, valid in a high-surface-density limit, in which quasi-liquid covers the surface.

After constructing and parameterizing the continuum model, we carry out simulations of an initially flat, one-dimensional ice surface, on a scale of 50 μm, as it grows due to vapor deposition over the course of a few seconds. We are particularly interested in mechanistic insights the model can provide as to how uniform growth comes about, and what it can tell us about the robustness of such growth. For example, the Nelson-Baker mechanism for faceted ice growth [*Nelson and Baker*, 1996] requires that the ice surface evolve in such a way that steps grow closer together at facet centers. Is the present continuum model consistent with this view? What additional insight can it provide? In essence, we hope that a model that explains faceted growth in the presence of vapor inhomogeneity can give us deeper insight into mechanisms of faceted growth.

This paper is organized as follows. In section 2 we describe our methodology and results from MD studies. In section 3 we describe the differential equations that comprise the continuum model, numerical strategies for solving it, and results from numerical solutions. Sections 4 and 5 provide discussion and conclusions.

2. MD Simulations

2.1. MD Methodology

An initial proton-disordered ice I_h crystal (hereafter, slab) was built by using Buch's algorithm [*Buch et al.*, 1998] and the NE6 water model [*Nada and van der Eerden*, 2003], composed of 2880 water molecules corresponding to 20 layers in the *x* direction and 12 bilayers in the *y* and *z* directions (each; see Figure 1).

The initial physical dimensions of the simulation box were 4.49, 4.67, and 4.40 nm in the *x*, *y*, and *z* directions. The initial ice crystal was prepared according to standard procedures reported in detail in *Gladich et al.* [2011, 2015]. A constant-pressure simulation (NpT) was performed at 0 bar for 2.5 ns during which the ice crystal was heated linearly from 0 K to the target temperature of 260 K, which corresponds to about 29 K below the melting temperature of NE6 water [*Abascal et al.*, 2006]. During the annealing process, a small time step of 0.1 fs was used to avoid ice crystal disorder and melting as the temperature was increased. Afterward, the *y* dimension of the simulation box was enlarged to 14 nm, exposing the two primary prismatic planes. Finally, starting from the ice/vapor slab, 20 ns of a constant volume (*NVT*) run was performed by using a time step of 2 fs at

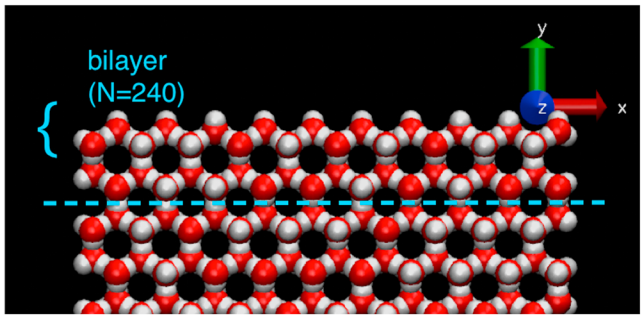

Figure 1. Initial configuration of the slab used in MD simulations, before annealing. Coordinate *x* coincides with the vector perpendicular to the secondary prismatic (11 $\bar{2}$ 0) facet. Coordinate *y* coincides with the vector perpendicular to the prismatic (10 $\bar{1}$ 0) facet and has extra space introduced between bilayers, creating an ice/vapor interface. Coordinate *z* coincides with the vector perpendicular to the basal (0001) facet (i.e., the crystallographic *c* axis). The entire slab consists of 12 bilayers (a bilayer is indicated with brackets) of 240 molecules in the *y* direction, for a total of 2880 molecules. The dashed horizontal line marks an arbitrary zero point for counting the number of molecules.

260 K, resulting in the formation of quasi-liquid layers at each ice/vapor interface after a few nanoseconds. The procedure described above has been shown to be a reliable protocol for simulation of ice interfaces using MD [*Girardet and Toubin*, 2001; *Muchová et al.*, 2011; *Gladich and Roeselová*, 2012; *Gladich et al.*, 2015].

The MD runs were performed by using GROMACS 5.0.7 [*Abraham et al.*, 2015] and a leapfrog integration method [*Hockney et al.*, 1974]. During the annealing NpT procedure, the Berendsen barostat [*Berendsen et al.*, 1984] with a coupling time of 2 ps was used to relax the crystal at zero pressure. In all the runs the temperature was kept constant at the desired value by using a stochastic-velocity-rescale thermostat [*Bussi et al.*, 2007], which is known to conserve the right ensemble properties, with a time constant of 0.1 ps. For nonbonded interactions (Coulombic and van der Waals) among water molecules, a cutoff of 1 nm was used, following the original parametrization for the NE6 water model [*Nada and van der Eerden*, 2003]. The particle mesh Ewald scheme [*Essmann et al.*, 1995] was employed to account for the long-range part of the Coulombic interaction, using a tolerance of 10^{-5}, fourth-order cubic interpolation, and 0.12 Fourier spacing. GROMACS offers a dispersion correction for the truncated part of the Lennard-Jones potential used to model the van der Waals interactions. However, due to inhomogeneities of the vacuum phase this correction was not used during the *NVT* runs with the slab configuration. Finally, the geometry of the water molecules was constrained during all MD runs by using the SETTLE algorithm [*Miyamoto and Kollman*, 1992]. This numerical setup is similar to that used in similar studies by using NE6, which has been shown to be numerically stable and conserve total energy [*Gladich et al.*, 2011; *Pfalzgraff et al.*, 2011; *Gladich et al.*, 2015].

Also indicated in Figure 1 is an (arbitrary) reference line that allows us to specify the total number of surface molecules, N_{tot}, that lie above it. In this paper, we will express this number in bilayer equivalents; for the slab shown in Figure 1, two bilayers lie above the reference line, comprising a total of 480 molecules; hence, $N_{TOT} = \frac{480}{240} = 2$ bilayer equivalents. As described in detail in previous MD work [*Gladich et al.*, 2011, 2015], this number may be further subdivided into ice- and liquid-like fractions, N_{ice} and N_{QLL}, using a tetrahedral order parameter. Briefly, for each water molecule (indexed by *i*), we calculate a tetrahedral order parameter defined by [*Errington and Debenedetti*, 2001]

$$q_i = 1 - \frac{3}{8}\sum_{j=1}^{3}\sum_{k=j+1}^{4}\left(\cos\left(\theta_{i,j,k}\right) + \frac{1}{3}\right)^2, \tag{1}$$

where indices *j* and *k* refer to oxygen atoms of nearest neighboring water molecules and the angle between the oxygen atom of molecule *i* and these two neighbors is given by $\theta_{i,j,k}$. This procedure yields relatively high values of q_i (close to 1) for water molecules belonging to the bulk ice phase and relatively low values of q_i for water molecules belonging to the liquid phase. Hence, a threshold, q_t, is selected such that for $q_i > q_t$ a water molecule is assigned to the crystal ice phase, whereas for $q_i < q_t$ the molecule is identified as liquid-like. Consistent with previous work, we use the NE6 threshold value of $q_t = 0.9264$ [*Gladich et al.*, 2011]. This criterion counts all subtetrahedrally coordinated water molecules (i.e., all exposed molecules) as liquid-like. As has been noted in the literature, this criterion could overestimate the number of liquid-like molecules at temperatures at which the QLL becomes so thin that all the interfacial molecules are frozen. However, this does not occur at the temperature used here (260 K), where the thickness of the QLL is about 0.38 nm and all exposed molecules are found to be liquid-like [*Gladich et al.*, 2011, 2015].

Much of the MD work carried out as part of this study was focused on characterizing the quasi-liquid thickness as one adds or removes molecules from the ice/vapor interface. Our starting point for this is the surface reported in previous studies, i.e., the simulated ice/vapor interface created by introducing a gap between bilayers of a slab, as shown in Figure 1. We designate the microsurface that results after annealing this configuration "Microsurface AB" (for annealed bilayer). Other microsurfaces are subsequently achieved through (1) transferring quasi-liquid molecules from the top of the slab to the bottom and (2) equilibrating the resulting surfaces, described next.

In transferring quasi-liquid molecules from the top of the slab to the bottom, we sought a method that would minimize the perturbation to the slab. The method we used will be designated hereinafter as thermal transfer through the periodic boundary (TTPB). In the TTPB method, we identify the topmost molecules of a given slab and add a vertical (+*y*) velocity component just large enough to dislodge those molecules from the surface. This guarantees that molecules removed from the top ice/vapor interface will be quasi-liquid, i.e., not part of the underlying ice lattice. These molecules subsequently travel at barely suprathermal speed through the vertical (*y* coordinate) periodic boundary and land on the lower surface of the slab a few picoseconds later. As we have argued elsewhere [*Neshyba et al.*, 2009], only a few tens of picoseconds are required for molecules deposited in this way onto the quasi-liquid layer to become indistinguishable, in terms of energy and orientation, from other quasi-liquid molecules. An animated example is given in the supporting information.

To allow equilibration of the resulting surfaces, trajectories were continued for an additional few nanoseconds after TTPB. As shown below, this time scale is sufficient to permit equilibration of the quasi-liquid/ice portions of the newly populated slab surfaces. Since the total number of molecules in the slab is kept constant in this method, a pair of microsurfaces result, one on the upper slab surface, from which molecules were (say) removed, and another on the lower slab surface, to which molecules were added. It is important to note that this procedure does not necessarily yield a top surface that contains less quasi-liquid or a bottom surface that contains more, since post-TTPB equilibration allows the surface to redistribute ice and quasi-liquid: a given microsurface could well equilibrate to a microsurface with *fewer* quasi-liquid molecules after addition of molecules, because of partial crystallization. Indeed, cyclic behavior is to be expected, in that after the transfer of a full bilayer of molecules (in the present slab, 240 molecules), the original configuration of Microsurface AB on both upper and lower slab surfaces must be reestablished.

Subsequent characterization of microsurfaces depended on the quantity desired. To characterize structural properties of a given microsurface (e.g., the average number of quasi-liquid molecules of the microsurface), the time scale was required to be long compared to the quasi-liquid/ice equilibration time scale (the latter being a few nanoseconds) but short compared to the vaporization/sublimation time scale (hundreds of nanoseconds; see discussion below), since the latter will tend to reestablish populations via spontaneous transfer of molecules from one surface to the other through the periodic, gas-phase boundary. Hence, after a microsurface had been established, the number of quasi-liquid and ice molecules was determined through equation (1), averaging values every 20 ps over 15–20 ns MD simulation.

In order to characterize the equilibrium vapor pressure of microsurfaces, sublimation/deposition events (i.e., spontaneous movement of water molecules from one slab surface to the other) were studied. These events are known to occur according to Poissonian statistics [*Neshyba et al.*, 2009], but at a rate of less than one per nanosecond for slabs of the size and temperature used in this study. This rate is slow compared to the quasi-liquid/ice equilibration time. Hence, our method for characterizing the equilibrium vapor pressure of microsurfaces was to carry out runs of ~20 ns, at the conclusion of which we noted any accumulation of molecules from one side of the slab to the other, and then restored the original pair of microsurfaces using the TTPB method described above. The rate of sublimation from each surface is proportional to the kinetic velocity, v_{kin}, which in turn is proportional to the equilibrium vapor pressure, P^*, via the Hertz-Knudsen formula [*Saito*, 1996],

$$v_{kin} = \frac{c_{sat}}{c_{solid}}\sqrt{\frac{kT}{2\pi m}} \propto P^* \tag{2}$$

where c_{solid} is the density of ice, c_{sat} is the density of water vapor in equilibrium with the solid, and m is the mass of a water molecule. It is worth noting that long trajectories (hundreds of nanoseconds) are required to achieve statistically meaningful absolute values of the vapor pressure using this method, and even so the

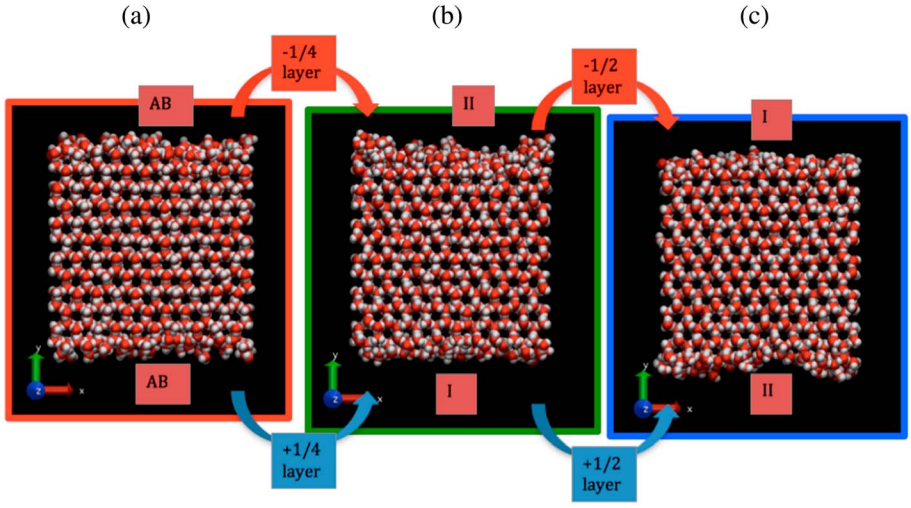

Figure 2. (a) Slab as annealed from the initial configuration shown in Figure 1, at a temperature of 260 K. The upper and lower bilayers are equivalent and labeled AB (for "annealed bilayer"). In this configuration, the upper slab is characterized as having 252 quasi-liquid molecules, hence $N_{QLL} = \frac{252}{240} = 1.05$ bilayer, while the lower slab has 246 quasi-liquid molecules, hence $N_{QLL} = \frac{246}{240} = 1.03$ bilayer. (b) After transferring 1/4 bilayer (~60 molecules) from the upper surface to the lower surface and allowing to equilibrate for ~20 ns. The resulting surfaces are called Microsurface I (lower surface) and Microsurface II (upper surface). (c) After transferring an additional 1/2 bilayer (~120 molecules) and equilibrating. The resulting surfaces are reversed, since removal of a net 3/4 bilayer is numerically equivalent to addition of a net 1/4, and vice versa.

results can vary among representations of the water-water intermolecular potential and deviate from experimental values by an order of magnitude [*Neshyba et al.*, 2009]. Instead, in this work, we employ equation (2) to determine relative supersaturations between microsurfaces of interest, using shorter trajectories, mainly for the purpose of determining the sign of difference between them. This is developed in context in the next section.

2.2. Results From MD

Figure 2a shows the slab with Microsurface AB on both upper and lower surfaces. Figure 2b results from transferring 1/4 bilayer (~60 molecules) from the upper surface to the lower surface and allowing the system to equilibrate for a few dozen nanoseconds. The lower surface of Figure 2a (Microsurface AB) is thereby transformed into a surface hereinafter designated Microsurface I, while the upper microsurface (also AB) is transformed into Microsurface II. Visual inspection suggests that Microsurface I is more ordered than Microsurface AB, while Microsurface II is less ordered; we shall return to this point below. Figure 2c results from transferring an additional 1/2 bilayer (~120 additional molecules) from the upper surface to the lower surface and allowing the system to equilibrate again. The lower surface is thereby transformed from Microsurface I to Microsurface II, and vice versa for the upper surface.

To visualize the evolution from Microsurface AB to Microsurfaces I and II, the number of molecules identified as quasi-liquid as the surface equilibrates during the transformation corresponding to Figures 2a and 2b is shown in Figure 3. The quasi-liquid of the lower side of the slab is initially (on a picosecond time scale) *thicker* than that for Microsurface AB, because the added water molecules are initially accommodated into the quasi-liquid. But on a nanosecond time scale, the quasi-liquid surface of this perturbed microsurface eventually becomes *thinner*, eventually to end up as Microsurface I. In contrast, the quasi-liquid thickness of the upper side of the slab is initially *thinner* than Microsurface AB (this thinning occurs on a time scale too short to be captured by the figure), but on a nanosecond time scale becomes *thicker* than Microsurface AB. This side eventually ends up as Microsurface II.

Figure 4 shows the results of multiple MD studies such as that which gave rise to Figure 3, with error bars indicating one standard deviation. Each marker displays the result of a particular TTPB perturbation and subsequent relaxation. The data suggest, visually, that N_{QLL} is indeed a nonconstant function of N_{tot}. To test this, we computed a reduced chi-square statistic, χ^2_{red} [*Bevington and Robinson*, 1993], under the assumption

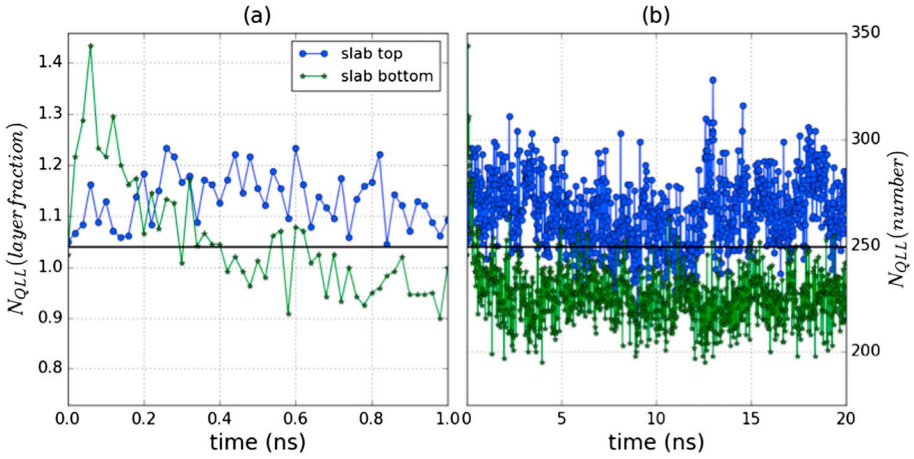

Figure 3. Time evolution of microsurface AB (upper and lower surfaces of Figure 2a) toward Microsurfaces II and I (upper and lower surfaces of Figure 2b, respectively), after transferring 50 molecules (slightly less than 1/4 bilayer) from Microsurface AB, slab top, to Microsurface AB, slab bottom, at time $t = 0$. The vertical axes correspond to the number of quasi-liquid molecules as a fraction of a single bilayer (left axis label) and as a number (right axis label), i.e., N_{QLL}(layer fraction) = N_{QLL}(number)/240. (a) Evolution in the first nanosecond, showing initial increases in both surfaces, but subsequent decrease in the quasi-liquid coverage of Microsurface I. (b) Evolution over 20 ns. The black solid horizontal line indicates the mean quasi-liquid thickness of Microsurface AB.

$N_{QLL} = \overline{N}$, where $\overline{N}$ is the mean quasi-liquid thickness for the data set. Doing so produced $\chi^2_{red} = 2.3$, which implies (to the extent that we consider $\chi^2_{red} > 1$) that $N_{QLL} = \overline{N}$ is a poor description given the estimated uncertainties. Alternatively, we can posit that the quasi-liquid depends sinusoidally on N_{tot},

$$N_{QLL} = \overline{N} - N^* \sin(2\pi N_{tot}), \tag{3}$$

where N^* parameterizes the variation around the mean. In this parameterization, the quasi-liquid portions of Microsurfaces I and II correspond to extreme thickness $\overline{N} \mp N^*$, respectively, in a continuum of microsurfaces that is periodic in N_{tot}. Two parameterizations of equation (3) are displayed in Figure 4. The solid line defines the "reference system" for the continuum model studies used throughout this paper; these parameters were arrived at based on a fit to an initial data set of MD results. The dashed line corresponds to a case for which parameters were optimized to match subsequent observations (i.e., the sinusoidal form matches the mean of the observed data points, and $N^* = 0.09$ yields a minimum mean-squared difference with respect to observations). We obtain in this way $\chi^2_{red} = 1.05$ for the optimized sinusoidal function, which we interpret to mean (since $\chi^2_{red} \approx 1$) that the extent of match between observations the sinusoidal model is in accord with the error variance.

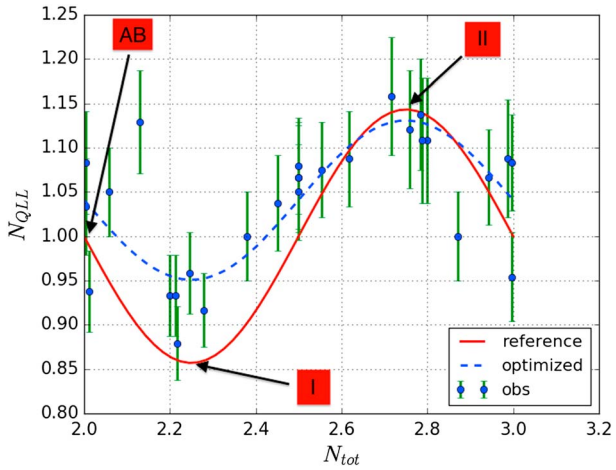

Figure 4. Dependence of QLL structure on total ice thickness determined in this work. Markers show MD-derived quasi-liquid coverage, in bilayer equivalents, with N_{tot} defined relative to the arbitrary zero indicated in Figure 1. The error bars correspond to one standard deviation in time series such as appeared in Figure 3. The continuous red line shows the sinusoidal approximation, equation (3), parameterized according to the reference system ($\overline{N} = 1$ and $N^* = 0.14$). A dashed line shows the same functional form after optimizing ($\overline{N} = 1.04$ and $N^* = 0.09$). Arrows point to Microsurfaces AB, I, and II.

MD-determined rates of sublimation were investigated in order to infer the relative equilibrium vapor pressures associated with microsurfaces, as determined by the Hertz-Knudsen

Table 1. Supersaturation Threshold Derived From MD-Derived Sublimation Events From a Slab Prepared by Perturbing Annealed Microsurface AB by Approximately 1/4 Bilayer

TTPB Relative to Microsurface AB	Time Interval (ns)	$v_{kin,MD,I}$ (molecules)	$v_{kin,MD,II}$ (molecules)	σ_o (%)
±60	0–20	3	12	300
	20–40	7	11	60
	40–60	9	5	−55
	0–60 (net)	19	28	47
±50	0–20	7	9	30
	20–40	5	6	20
	40–60	3	7	130
	0–60 (net)	15	22	50

formula (equation (2)). The relative difference between Microsurfaces I and II is here designated the *threshold supersaturation*,

$$\sigma_o = \frac{P_{II}^* - P_I^*}{P_I^*} = \frac{v_{kin,MD,II} - v_{kin,MD,I}}{v_{kin,MD,I}}, \tag{4}$$

where $v_{kin,MD,I}$ is the rate of departure of water molecules from Microsurface I to the vapor phase and similar for $v_{kin,MD,II}$. Supersaturation thresholds are displayed in Table 1, showing results after a slab initially annealed as Microsurface AB was perturbed by TTPB movement of approximately 1/4 bilayer from the top to the bottom of the slab, followed by a relaxation of 2–5 ns. Thus, after TTPB of exactly 1/4 bilayer (60) molecules, the top of this slab approximates Microsurface II and the bottom Microsurface I. Over the next 60 ns, sublimation events from these surfaces were tracked, rebalancing every 20 ns to restore the desired deficit/excess (also by TTPB). While these trajectories are too short to characterize a supersaturation threshold value with high precision, the results strongly suggest a higher equilibrium vapor pressure for Microsurface II compared to Microsurface I, hence a positive value of σ_o. This conclusion appears to hold even when the microsurfaces are prepared with deficit/excess of slightly less than 1/4 of a bilayer imbalance (50 molecules instead of 60; see the second half of Table 1).

Because of the aforementioned uncertainty in values of σ_o obtained in this way, the values used in the continuum model were chosen according to other criteria, as described in the next section.

2.3. A Qualitative Growth Scenario Based on MD

On the basis of the foregoing, we can imagine that QLL structure and vapor pressure act in concert to yield the following growth scenario. We shall assume for the moment that the ambient vapor pressure is large enough to exceed the equilibrium vapor pressure of even the most volatile microsurface of the surface, Microsurface II. Mathematically, this can be expressed as $\sigma_I > \sigma_o$, where σ_I is the supersaturation relative to Microsurface I and σ_o is the threshold supersaturation defined in equation (4). It is also convenient (although arbitrary) to imagine that the surface is initially structured as Microsurface AB, i.e., at the extreme left of Figure 4. Because the ambient supersaturation relative to this microsurface is positive, net deposition from the vapor phase will occur, causing an accumulation of water on the surface: an increase in N_{tot}. This moves the state of the system to the right in Figure 4. We can imagine a transient increase in N_{QLL}, but as quasi-liquid/ice equilibration occurs (which will occur on a nanosecond time scale), we see from Figure 4 that N_{QLL} must decrease. That is, the deposition of water molecules atop Microsurface AB induces a rearrangement in the quasi-liquid layer that leads to a partial crystallization and a net reduction in quasi-liquid. This process also hastens the pace of growth, since the equilibrium vapor pressure of the newly formed, partially crystalized microsurface is lower than that of Microsurface AB. This process continues until N_{QLL} is at a minimum; i.e., the surface arrives at Microsurface I in Figure 4. At this point, the rate of accumulation is fastest, since the equilibrium vapor pressure of Microsurface I is the smallest of all the microsurfaces. Once N_{tot} exceeds this point, continued accumulation of water from the vapor (increasing N_{tot}) takes the surface toward Microsurface II, all the while also increasing N_{QLL} and slowing the rate of growth. At Microsurface II, the rate of accumulation is slowest, since the equilibrium vapor pressure of Microsurface II is the largest of all microsurfaces. Subsequently, a situation similar to the initial one is resumed: continued net deposition from the vapor phase will cause an increase in N_{tot} and (through partial crystallization) a decrease in N_{QLL}. This will continue until Microsurface AB is once again achieved and the growth cycle begins anew.

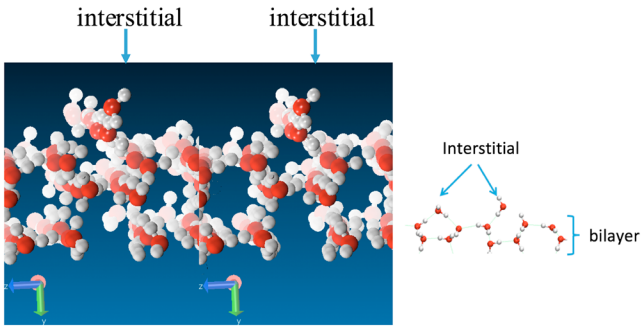

Figure 5. Interstitial and lattice positions of the prismatic surface of ice, seen from the *x* direction. (left) Stereo view of a snapshot of Microsurface I. Glossy rendering indicates molecules occupying interstitial positions; diffuse rendering indicates molecules occupying lattice positions. (right) Profile showing orientation of interstitial admolecules, adapted from *Gladich et al.* [2015], see also Figure S1.

Because of the key role played in the scenario by the threshold supersaturation, σ_o, we have sought to understand the mechanism by which Microsurface I achieves a minimum equilibrium vapor pressure and chemical potential. In other words, why does Microsurface I exhibit enhanced stability? Figure 5 shows a magnified, stereoscopic view of the quasi-liquid bilayer derived from an MD simulation; it corresponds to the lower surface of Figure 2b but with axes inverted to display the Microsurface I at the top of the figure. A row of molecules occupying interstitial sites is highlighted with glossy rendering. There are 60 such sites available on a slab of the dimensions studied here, i.e., 1/4 bilayer. A plausible interpretation therefore is that the stability of Microsurface I is due to the optimal occupation of available interstitial sites offered by the underlying quasi-liquid bilayer. This interpretation must be regarded as tentative, however, pending more detailed investigations.

Looking forward to the continuum model, it is important to note that the processes described in this section take place on an MD time scale: equilibration of the quasi-liquid layer with the underlying ice lattice on the order of a few nanoseconds, and equilibration of the quasi-liquid with the vapor on the order of a few hundred nanoseconds. To this insight, we can add one more from prior work: MD simulations of ice slabs have shown that lateral (in-plane) diffusion of quasi-liquid molecules at the ice slab/vapor interface scales in accordance with Einstein's mean-square-displacement formula (i.e., the mean square displacement is a linear function of time) [*Gladich et al.*, 2011]. A coarse-grained model, in contrast, by construction will employ a much larger time step, on the order of microseconds. These observations, in turn, justify the coarse graining of microsurface dynamics in which mesoscopic diffusion is described by a conventional diffusion equation, and in which quasi-liquid/ice and quasi-liquid/vapor equilibration may be incorporated as parameterized, effectively instantaneous processes. These ideas are developed formally in the next section.

3. The Continuum Model

3.1. Definition of the Continuum Model

3.1.1. Mathematical Structure of the Model

The continuum model developed here is a mesoscopic model that provides for diffusion of the quasi-liquid part of the ice/vapor interface, source terms describing spatially inhomogeneous deposition of water from the vapor phase, and dynamic partitioning of the ice and quasi-liquid components of the surface. These features are implemented by

$$\frac{\partial N_{\mathrm{tot}}}{\partial t} = D\nabla^2 N_{\mathrm{QLL}} + \sigma_m v_{\mathrm{kin}}, \tag{5a}$$

$$\frac{\partial N_{\mathrm{QLL}}}{\partial t} = D\nabla^2 N_{\mathrm{QLL}} + \sigma_m v_{\mathrm{kin}} N'_{\mathrm{QLL}}, \tag{5b}$$

$$\frac{\partial N_{\mathrm{ice}}}{\partial t} = \sigma_m v_{\mathrm{kin}} \left(1 - N'_{\mathrm{QLL}}\right), \tag{5c}$$

where the dynamical variables of the model are N_{tot}, the total thickness of the ice/vapor interface (in bilayer equivalents); N_{QLL}, the thickness of the quasi-liquid part of the interface; and N_{ice}, the thickness of the ice-like part. Initial configurations were constant values across the facet, while "trajectories" consisted of the time evolution of each, i.e., $N_{\mathrm{tot}}(x,t)$, $N_{\mathrm{QLL}}(x,t)$, and $N_{\mathrm{ice}}(x,t)$, where t specifies the time and x specifies the location along the facet. A zero-dimensional version of the continuum model is achieved setting $D = 0$, which removes all position dependence; in the one-dimensional case, periodic Dirichlet boundary conditions were used.

Remaining quantities appearing in equations (5a), (5b), (5c) are N'_{QLL} (the partial derivative of N_{QLL} with respect to N_{tot}), which controls the partitioning at the surface between quasi-liquid and ice-like fractions; D, the surface self-diffusion coefficient of the ice/vapor interface; v_{kin}, the kinetic growth velocity; and σ_m, the microscopic supersaturation, which depends on N_{QLL}, N_{ice}, and N_{tot}.

Additional details about these are the following:

1. N_{tot} is defined relative to a baseline of ice below the surface. This baseline is arbitrary in terms of the number of bilayers but otherwise conforms to the conventional definition of a bilayer, e.g., of a prismatic facet [*Buch et al.*, 1998; *Petrenko and Whitworth*, 1999; *Shultz et al.*, 2014]. The baseline used here is shown in Figure 1.
2. N_{QLL} relates to the atomistic level in that it corresponds to the thickness of liquid-like molecules defined by the tetrahedral order parameter described above [*Errington and Debenedetti*, 2001; *Gladich and Roeselová*, 2012]. It is parameterized here as equation (3), hence $N'_{QLL} = \frac{\partial N_{QLL}(N_{tot})}{\partial N_{tot}} = -2\pi N^* \cos(2\pi N_{tot})$.
3. N_{ice} can be computed from equation (5c) simultaneously with equations (5a) and (5b), as a third dynamical variable. However, it is more efficient to solve equations (5a) and (5b) first and compute N_{ice} algebraically by using $N_{tot} = N_{QLL} + N_{ice}$.
4. $D\bar{\nabla}^2(\ldots)$, the diffusion operator appearing in the model, operates only on the thickness of the quasi-liquid portion of the ice/vapor interface, in keeping with the notion that diffusion of the underlying ice is small in comparison. We rely on temperature-dependent MD results for specification of D [*Gladich et al.*, 2011].
5. $\sigma_m v_{kin}$ is the source term for the total ice/vapor interface, representing the deposition of water vapor. Its components are as follows:

v_{kin}, the kinetic growth velocity. v_{kin} is temperature-dependent and can be calculated from the Hertz-Knudsen formula (2).

σ_m, referred to here as the microscopic supersaturation to indicate its dependence on location (representing spatial inhomogeneities of the vapor field) as well as the instantaneous microscopic structure of the ice/vapor interface at that location. It is convenient to parametrize σ_m in terms of the current microsurface. Thus, it is necessary to specify how surface properties depend on microsurfaces intermediate between Microsurfaces I and II. The model characterizes this as a *microscopic transition parameter*,

$$m \equiv \frac{N_{QLL} - (\overline{N} - N^*)}{2N^*}. \tag{6}$$

The microscopic transition parameter is an implicit function of position and time, since $N_{QLL} = N_{QLL}(x,t)$. This equation specifies that the surface state for which the quasi-liquid is thinnest (Microsurface I) is characterized by $m = 0$, while the surface state for which the quasi-liquid is thickest (Microsurface II) is characterized by $m = 1$. Quantities below that are functions of m are likewise implicit functions of position and time.

With the above definition, the equilibrium water vapor pressure associated with a given location on the facet, a quantity we designate as P^*_m, depends linearly on the microscopic transition parameter according to

$$P^*_m = P^*_I + m \times (P^*_{II} - P^*_I), \tag{7}$$

so that $P^*_{m=0} = P^*_I$ and $P^*_{m=1} = P^*_{II}$. Combining this equation with equation (4), we can rewrite the equilibrium water vapor pressure as

$$P^*_m = P^*_I \times (1 + m\sigma_o). \tag{8}$$

We write the microscopic supersaturation as

$$\sigma_m \equiv \frac{P_{amb,x} - P^*_m}{P^*_m}, \tag{9}$$

where $P_{amb,x}$ represents the ambient water vapor pressure at location x. Substituting equation (8), we have

$$\sigma_m = \frac{P_{amb,x} - P^*_I \times (1 + m\sigma_o)}{P^*_I \times (1 + m\sigma_o)}. \tag{10}$$

Using the above definitions, we have

$$\sigma_m = \frac{\sigma_I - m\sigma_o}{1 + m\sigma_o}. \tag{11}$$

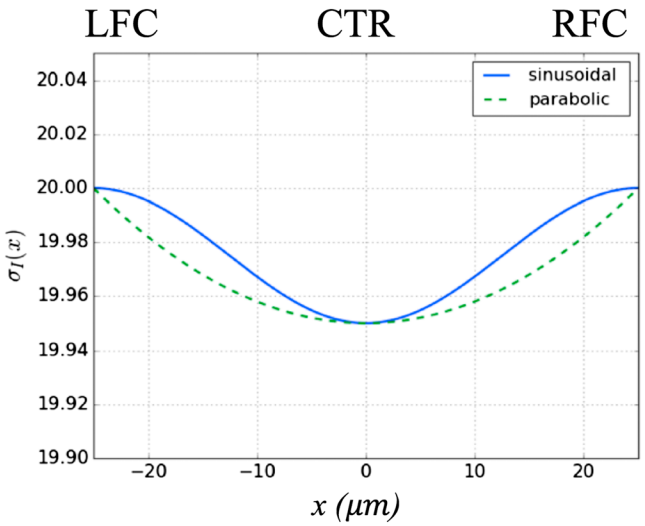

Figure 6. Imposed water vapor field, $\sigma_I(x)$, for the reference system, showing sinusoidal and parabolic shape functions for the water vapor inhomogeneity, both parameterized by $c_r = 0.25$ % (see equations (13)–(15) in the text). LFC, CTR, and RFC refer to left facet corner, facet center, and right facet corner, respectively.

In order to calculate σ_m therefore we need σ_o (an intrinsic function of the ice vapor interface derived from MD simulations, discussed in section 2), m (obtained from the dynamical variables, as shown in equation (6)), and σ_I (discussed next).

σ_I corresponds to the supersaturation immediately above the ice surface, often designated σ_{surf} in the literature. We use the subscript "I" here to emphasize that supersaturation must be specified relative to the equilibrium vapor pressure of some reference state, which is not unique at the microscopic level: according to the results of section 2, microsurfaces vary in equilibrium vapor pressure from a low of P_{I}^* to a high of P_{II}^*. The choice of Microsurface I as this reference,

$$\sigma_{\text{I}} \equiv \frac{P_{\text{amb},x} - P_{\text{I}}^*}{P_{\text{I}}^*} \tag{12}$$

conforms to the convention that a surface supersaturation of zero coincides with the minimum ambient supersaturation required to prevent net ice ablation. The spatial dependence of σ_{I} is functionalized as

$$\sigma_{\text{I}}(x) = \sigma_{\text{I,corner}} \times f_{\text{inhomog}}(x), \tag{13}$$

where $\sigma_{\text{I,corner}}$, a scalar, specifies the supersaturation at the boundaries, or corners, of the simulation box, i.e., at $x \pm L$. The function $f_{\text{inhomog}}(x)$ specifies the shape of the inhomogeneous water vapor field, and in general is not known. One choice is $f_{\text{inhomog}}(x) = f_{\text{sinusoidal}}(x)$, an inhomogeneity field given by

$$f_{\text{sinusoidal}}(x) = 1 - c_r\left[1 + \cos\left(\frac{x}{L}\pi\right)\right]/2. \tag{14}$$

Another is $f_{\text{inhomog}}(x) = f_{\text{parabolic}}(x)$, a field given by

$$f_{\text{parabolic}}(x) = c_r\left(\frac{x}{L}\right)^2 + (1 - c_r). \tag{15}$$

In both expressions, c_r is a parameter that controls the reduction of water vapor at facet center relative to facet corners. For example, $c_r = 0.0025$ corresponds to a reduction of 0.25% supersaturation at facet center (see Figure 6; here L is 25 μm).

3.1.2. Model Input Parameters

Table 2 summarizes the parameters chosen as a focus for this study, which we will refer to as the reference system.

The first two input parameters, σ_o and c_r, were chosen iteratively, i.e., on the basis of model results. Thus, they are described immediately following model output parameters. The rest of the parameters were obtained from physical considerations or experiment. The value of the surface self-diffusion coefficient D was based on prior MD simulations at this temperature [*Gladich et al.*, 2011]. We chose a facet size of 50 μm, i.e., $L = 25$ μm, as representative of cirrus ice crystals. At a temperature of 260 K, the kinetic velocity, v_{kin}, was chosen to conform with the value obtained from the Hertz-Knutsen formula given in equation (2); a nominal layer thickness of 0.3 nm was used to convert this value into a bilayer velocity. The precise value chosen for the imposed supersaturation at the corners of the facet, $\sigma_{\text{I,corner}}$ (corresponding to locations right facet corner (RFC) and left facet corner (LFC) in Figure 6) was arbitrary, but it lies within the range of conditions for which experimental results are available. $\overline{N}$ and N^* are chosen based on the MD results described in section 2. Since

Table 2. Parameters Defining the Reference System of the Continuum Model

σ_o	c_r (%)	D ($\mu m^2\ \mu s^{-1}$)	L (μm)	v_{kin} ($\mu m\ s^{-1}$)	v_{kin} (bilayer μs^{-1})	$\sigma_{I,corner}$	$\overline{N}$ bilayer	N^* bilayer	$f_{inhomog}(x)$
0.19	0.25	2×10^{-4}	25	49	0.16	0.20	1	0.14	$f_{sinusoidal}(x)$

initial model runs were carried out before the optimized parameterization shown in Figure 4 was available, the standard model parameterization was used; however, our qualitative results and conclusions do not depend substantially on this choice.

3.1.3. Model Output

Time-averaged values of the growth rate and the accommodation coefficient are the model outputs of primary interest here. The growth rate at any given time and position in a simulation is given by

$$v_{x,t} = \frac{\partial N_{tot}}{\partial t}, \tag{16}$$

which permits us to define a microscopic accommodation coefficient, $\alpha_{x,t}$, according to the usual formula for the accommodation coefficient,

$$v_{x,t} = \alpha_{x,t} v_{kin} \sigma_I, \tag{17}$$

where σ_I was parametrized earlier.

Values of $\alpha_{x,t}$ and $v_{x,t}$ depend on position and time, as indicated by the subscripts, but experimental analogs of these quantities are generally given as time-averaged, steady state quantities. To average steady state quantities from the model, it is usually sufficient to consider any single cycle of layer growth. These averages will be indicated by the notation $\langle \ldots \rangle_t$. For example, the average growth rate at a facet corner is designated $\langle v_{corner,t} \rangle_t$ and is obtained by averaging equation (16) over a single cycle of steady state growth. Time-averaged local supersaturation at a corner is similarly designated $\langle \sigma_{\delta,corner,t} \rangle_t$. The mean accommodation coefficient at a corner is given by

$$\langle \alpha_{corner,t} \rangle_t = \frac{\langle v_{corner,t} \rangle_t}{v_{kin}\ \sigma_{I,corner}}, \tag{18}$$

where $\sigma_{I,corner}$. is the supersaturation at the corner (a scalar) introduced in equation (12). Behavior of this quantity as a function of supersaturation is of interest in relation to experimental results. This is because, according to nucleation theory, layer growth governed by two-dimensional nucleation is expected to yield an accommodation coefficient given by

$$\alpha_s = A_{Nuc}\ \exp\left(-\sigma_{o,Nuc}/\sigma_I\right), \tag{19}$$

where A_{Nuc} and $\sigma_{o,Nuc}$ may be temperature- and facet-dependent but are not functions of the supersaturation [*Saito*, 1996]. Indeed, linearity of $\ln(\alpha_s)$ as a function of $1/\sigma_I$ is taken as evidence that nucleation theory governs the process of nucleation and allows the calculation of the edge free energy [*Libbrecht*, 2003b]. Although nucleation theory plays no part in the derivation of the atomistic/continuum model presented here, it is regardless of interest to compare accommodation coefficients from the model ($\langle \alpha_{corner,t} \rangle_t$) to experimental values (α_s) as a way of gauging limitations of the model. Moreover, the physical interpretation of $\sigma_{o,Nuc}$ is that of a nucleation supersaturation threshold, manifested experimentally as a finite water vapor supersaturation that must be imposed before growth is observed. It is therefore to be expected that it will be related to the microscopic supersaturation, σ_o, used in the continuum model.

It is useful to have a proxy that indicates, in some way, the ease with which the system accomplishes uniform growth. Here we have chosen the *bilayer thickness difference* between facet center and corner, designated N_{SS} at steady state, as such a proxy. A small value of N_{SS} corresponds to a flatter facet and more facile formation of a steady state. We should add that even very large values of N_{SS} could correspond to uniform growth, provided a steady state is achieved, but the resulting facet would appear distorted, i.e., as a hollowed facet.

3.1.4. Model Input Parameters Chosen Iteratively

Given the large uncertainties in MD-derived values of the threshold supersaturation, σ_o, described above, we treat it here as an adjustable parameter of the model. It turns out that, within the model, the accommodation efficiency depends mainly on σ_o. Therefore, the precise value of σ_o was chosen to yield a time-averaged accommodation

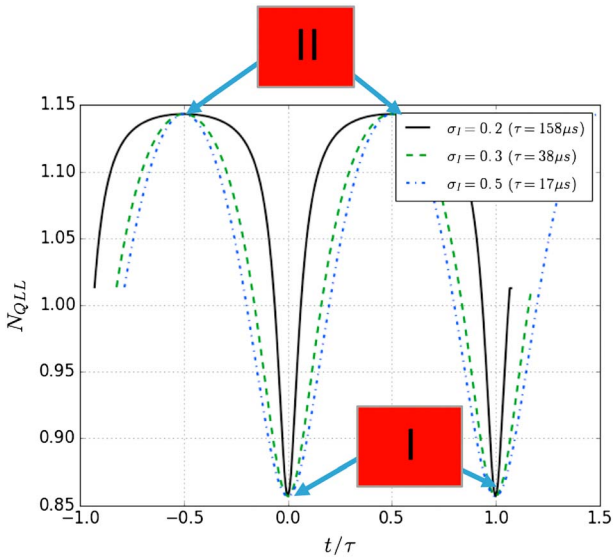

Figure 7. Time evolution of quasi-liquid thickness for the zero-dimensional reference system (solid black curve), and two others parameterized with larger surface supersaturation. Boxes refer to Microsurfaces I and II.

coefficient ($\langle \alpha_{\mathrm{corner},t} \rangle_t$) approximately equal to the experimental value under conditions specified by the other parameters of the standard system [*Libbrecht*, 2003b].

A second parameter chosen iteratively was c_r, which controls the inhomogeneity of the vapor field. We are interested in the largest possible value of c_r that can be imposed for which the model can still produce numerically stable steady state solutions. We discuss the boundary between stable and unstable solutions in the next section.

3.2. Methodology of Continuum Model Calculations

All results presented here used a simulation box containing $N_x = 500$ cells spanning physical dimensions $x = -L$ to $+L$, with reflection symmetry at $x = 0$, and periodic boundary conditions. The differential operator was discretized to produce a set of N_x ordinary differential equations, which were then solved by the stiff ordinary differential equation solver found in ODEPACK, accessed through python's numpy package [*Hindmarsh*, 1983; *Oliphant*, 2006]. Although ODEPACK adjusts the integration time step internally to achieve a normalized tolerance of 1.5×10^{-8}, trajectory integration was interrupted every 5 μs to correct any numerical drift away from equation (3), which in any case was quite small. For most simulations, a spatial step size of 0.1 μm was used, the exception being trajectories intentionally designed to study the behavior of the system as a function of the facet size. Initial configurations were a constant (arbitrary) number of ice-like layers, N_{ice}, preequilibrated with a quasi-liquid depth, N_{QLL}, according to equation (3).

3.3. Insights From the Zero-Dimensional Case

We next examine solutions to the continuum model in which the independent variable, x, is a single point, which we will refer to here as the zero-dimensional case. This is equivalent to setting $D = 0$ in equations (5a), 5b, 5c. Our purpose is to determine what insights we may derive from these results, before proceeding to the one-dimensional model.

First, we consider in Figure 7 the time dependence of quasi-liquid thickness over two layer cycles of the reference system, along with two comparison systems with larger supersaturation. The horizontal axis has been aligned and scaled according to $t' = t\langle v_t \rangle_t = t/\tau$, so that a complete a layer cycle occurs in the range $t' = 0$ to 1 in each case. Actual periods are indicated in the legend. A striking feature of the curves in Figure 7 concerns the structural differences among these curves. If we compare the solid curve to the dashed/dotted curves, we see that the solid curve (which corresponds to a value σ_I approaching σ_o, the critical supersaturation) is rather flat at the top of the graph, meaning it spends much of the time in a state close to Microsurface II. In contrast, the dashed and dash-dotted curves (which correspond to values σ_I well in excess of σ_o) are flatter at the *bottom* of the graph, meaning they spend relatively more time similar to Microsurface I.

As discussed above, steady state bulk accommodation coefficients, designated $\langle \alpha_t \rangle_t$, are a measure of the efficiency with which a growing ice surface captures water vapor and converts it to ice. These values, obtained from averaging growth over a complete layer cycle, are displayed in Figure 8, note the vertical log scale.

It is clear from the figure that the trend in $\langle \alpha_t \rangle_t$ is qualitatively consistent with the expectations articulated above, namely, that accommodation efficiency increases with increasing supersaturation. Also shown in Figure 8 are experimental values, here designated as α_s; these were generated by using equation (19) with parameters reported by *Libbrecht* [2003b] for vapor-deposited ice growth of prismatic facts. We first note that

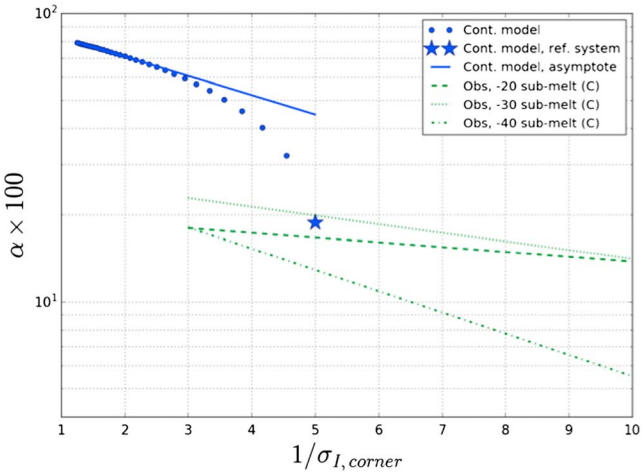

Figure 8. Accommodation graph for ice. Time-averaged accommodation coefficients, $\langle \alpha_{\mathrm{corner},t} \rangle_t$, of the steady state of the reference continuum model (blue asterisk), extended over a range of supersaturations (blue circles). Also shown are experimental values of the accommodation coefficient, α_s, for the prismatic facet over a range of submelt temperatures, obtained via equation (19) [*Libbrecht*, 2003b].

the approximate agreement with experiment that occurs at a submelt temperature of -30℃ and ambient supersaturation $\sigma_{\mathrm{I}} = 0.2$, was engineered by tuning the value of σ_o in the reference system. Hence, the proximity of the blue asterisk to experimental curves cannot be considered a merit of the model, except inasmuch as it was *possible* to tune the model so that this agreement could be achieved. More telling is how the model behaves around this point. While the locus of points produced by the model does not form a straight line, there is an apparent asymptotic linearity (at large supersaturation) in the model. The negative slope of this asymptote (as shown by the solid green line) is 0.15, which is comparable to the range of observed $\sigma_{o,\mathrm{Nuc}}$ values (0.04 to 0.17) for the experimental temperature range displayed (-20 to -40℃). Our conclusion is that σ_o is a microscopic analog to $\sigma_{o,\mathrm{Nuc}}$, albeit an imperfect one in that σ_o represents a sharp cutoff in the continuum model, whereas $\sigma_{o,\mathrm{Nuc}}$ does not.

3.4. Results From the One-Dimensional Continuum Model

We next turn to a consideration of solutions to the one-dimensional model (equations (5a), (5b), (5c)). Initial configurations were specified as a constant (arbitrary) number of ice-like layers, N_{ice}, preequilibrated with a quasi-liquid depth, N_{QLL}, according to equation (3). Figure 9 shows typical snapshots of the reference system at different times. The left-hand side of the figure shows the initial configuration. The middle part shows the system after enough time has evolved to generate three steps; these steps form initially at corners because the imposed supersaturation is greater there. These steps are not static, but traverse across the face toward the center on a time scale of hundreds of microseconds. The right-hand side of the figure shows the system after a simulation time long enough for the system to arrive at steady state. Steps still propagate from corner to center (see the supporting information for an animated version of these data), and the height of the surface keeps growing, but now the overall curvature of the surface remains constant.

From graphics such as this, one can also infer a relationship between steps and terraces on the one hand, and microscopic structure on the other. Since Microsurface I appears with a minimum quasi-liquid thickness, it is evident that it occurs in these trajectories in the vicinity of *steps*. Likewise, since Microsurface II appears with a maximum quasi-liquid thickness, it appears in these trajectories in the vicinity of *terraces*. Hence, steps are surfaces with lower equilibrium vapor pressure and chemical potential, while terraces are surfaces with large equilibrium vapor pressure and chemical potential. It is also clear from the figure that in all cases, the surface spends more time as a terrace (hence, similar to Microsurface II) than as a step (similar to Microsurface I). Lastly, we note that the stair-step pattern at steady state exhibits a distinct narrowing of terrace widths as one proceeds from facet center out to facet corners.

Table 3 displays output parameters of this steady state. We see that the one-dimensional model grows more slowly than the corresponding zero-dimensional model. The difference is nearly 3%, much greater than reduction in surface supersaturation at facet center, c_r (0.25%).

Figure 10 shows the properties of transient solutions as the system evolves toward a steady state. The system parameters for this trajectory coincide with the reference system, with the exception that the supersaturation, $\sigma_{\mathrm{I,corner}}$, is slightly higher. The left-most part of the curve corresponds to the initial flat configuration, corresponding to Figure 9a. By the time $N_{\mathrm{ice}} = 125$ layers have formed, four steps have formed, corresponding to

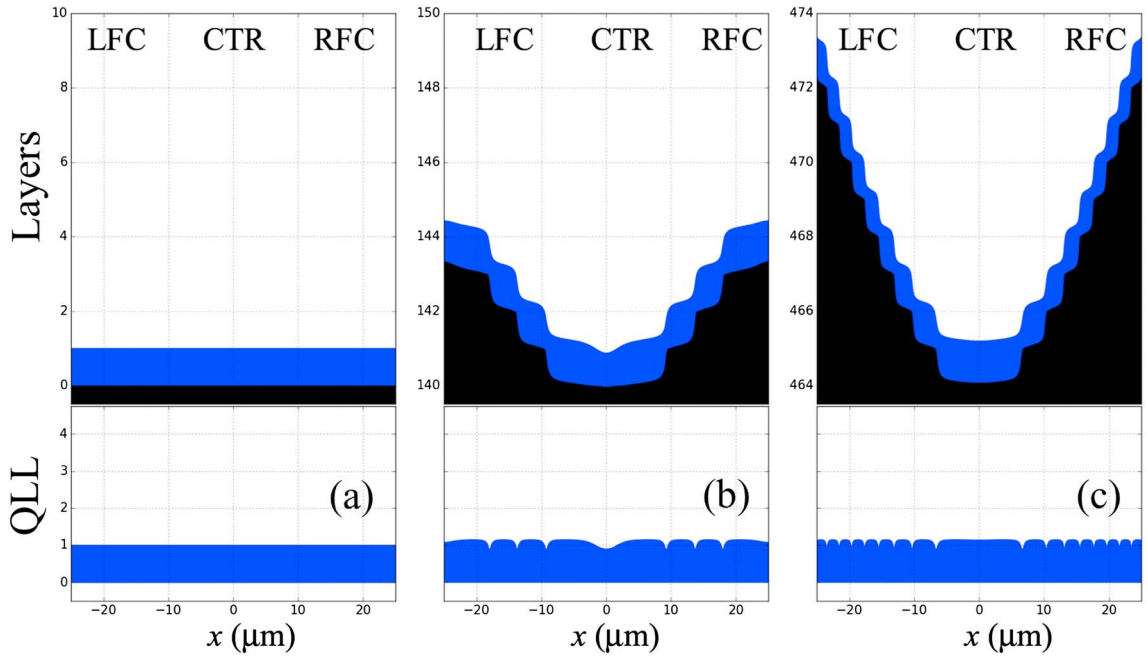

Figure 9. Structure of the ice surface at (a) 0, (b) 23, and (c) 75 ms after the beginning of a simulation of the standard system. Each panel runs from the left facet corner (LFC), through the facet center (CTR), to the right facet corner (RFC). Ice thickness, N_{ice}, is shown in black; total thickness, N_{tot}, overlaid in blue. The lower blue curves show the quasi-liquid thickness alone. N_{trans} is defined as the number of steps leading from facet center to facet corner at any given point in a simulation, while N_{SS} is this number at steady state. Here Figures 9a and 9b are characterized by $N_{trans} = 0$ and $N_{trans} = 3$. Since the system has reached steady state in Figure 9c, $N_{SS} \approx 8$. An animated version of the steady state is supplied in the supporting information.

Figure 9b. By the time 400 ice layers have formed, the system has arrived at a steady state with nine layers. This is slightly greater than the steady state of the reference system shown in Figure 9c because, with a higher supersaturation, excess growth at corners is slightly greater compared to the reference system. The figure strongly suggests that steady state solutions are a result of a locking-in mechanism.

It is worth emphasizing that this behavior, e.g., the spontaneous emergence of steady states, is not unusual for nonlinear systems such as the model constructed here, often involving feedback. In the language of nonlinear systems theory, such dynamic steady states are described as stable limit cycles, or attractors, i.e., a subset of the phase space of the system, toward which a range of initial conditions spontaneously evolve [*Nicolis et al.*, 1977; *Ye and Lo*, 1986; *Curto and Itskov*, 2008].

We address next the question of robustness of the cycle by examining the range of parameters that lead to steady state solutions. Figure 11 examines variations in N_{SS} that occur when parameters of the model are changed away from the reference system. The abscissa, $\frac{v_{kin} L^2 c_r^{\beta} \sigma_{l,corner}}{D}$, is motivated by dimensional analysis, with the exception of the exponent, β, of the inhomogeneity parameter, which cannot be deduced on dimensional grounds. Qualitatively, these results show that uniform growth is promoted (as indicated by smaller N_{SS}) by large self-diffusion coefficient, slow growth rates (small kinetic velocity and supersaturation), and small crystal size (small L). Lower values of N_{SS} for the parabolic case indicate a greater readiness to form steady states, compared to the sinusoidal case.

Quantitatively, the data indicate that the dependence of N_{SS} is approximately consistent with the empirical relationship

$$N_{SS} \approx M \frac{v_{kin} L^2 c_r^{\beta} \sigma_{l,corner}}{D} + B, \quad (20)$$

where M, B, and β are empirically determined from a least-squared fit to the data for the sinusoidal and parabolic vapor fields (separately).

Table 3. Model Output Results for the Reference Steady State Solution

$\langle v_{corner,t} \rangle_t$ (μm/s)	$\langle v_{zero\text{-}order,t} \rangle_t$ (μm/s)	$\langle \alpha_{corner,t} \rangle_t$	N_{SS} (bilayers)
1.85	1.90	0.19	8.2

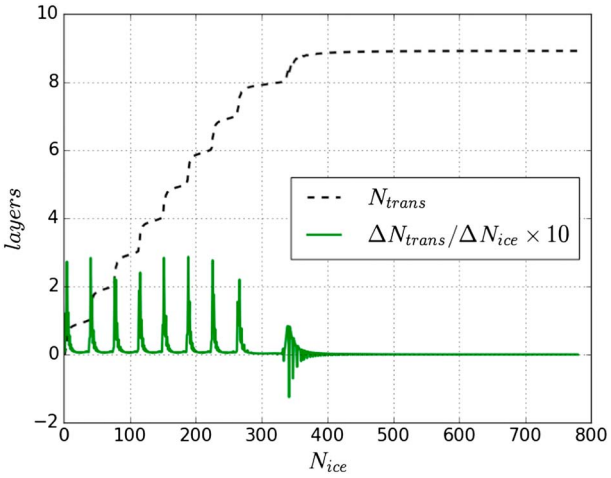

Figure 10. Time evolution of N_{trans}, the transient difference in the number of ice layers between facet corner and facet center (dashed black curve). The solid green curve shows the slope of this curve. Each peak in the latter signals the addition of one additional step across the facet.

Parameters derived in this way are $M \approx 0.0027$, $B \approx 2.9$ for the sinusoidal case, and $M \approx 0.0025$, $B \approx 1.6$ for the parabolic case. $\beta = 0.65$ for both cases.

Ranges of parameters contributing to the variation in the figure are shown in Table 4. It is instructive to compare these ranges to conditions under which faceted growth is observed. The minimum diffusion coefficient for which steady states were found coincides approximately with a submelt temperature −39℃ for NE6 water [*Gladich et al.*, 2011]. This is lower than the threshold temperature for which quasi-liquid coverage is one bilayer for the prismatic facet of ice, −35 ℃ [*Gladich et al.*, 2015]. Since larger D facilitates faceted growth, we conclude that the range of diffusion coefficients supporting faceted growth spans the entire range over which the continuum model is expected to apply, i.e., −35 ℃ to melting. The range of crystal sizes, L, coincides with typical cirrus cloud particles, although on the high end the model predicts that facets will give way to unbound corner growth. A similar comment applies to the range of kinetic velocities, v_{kin}. Regarding the inhomogeneity parameter, c_r, the maximum value seems rather small: when c_r exceeds only 0.7%, trajectories of the model become numerically unstable. Rudimentary analysis, employing the fact that the diffusivity of water vapor through air is ~10^5 faster than that of quasi-liquid on ice surfaces, suggests $c_r < 1\,\%$ under typical atmospheric conditions, although this requires verification. Finally, we recognize that the surface supersaturations ($\sigma_{I,corner}$) listed in Table 4 are much higher than occur in typical cirrus clouds, where growth is typically diffusion-limited, although such conditions can be reached in even modestly low-pressure laboratory conditions.

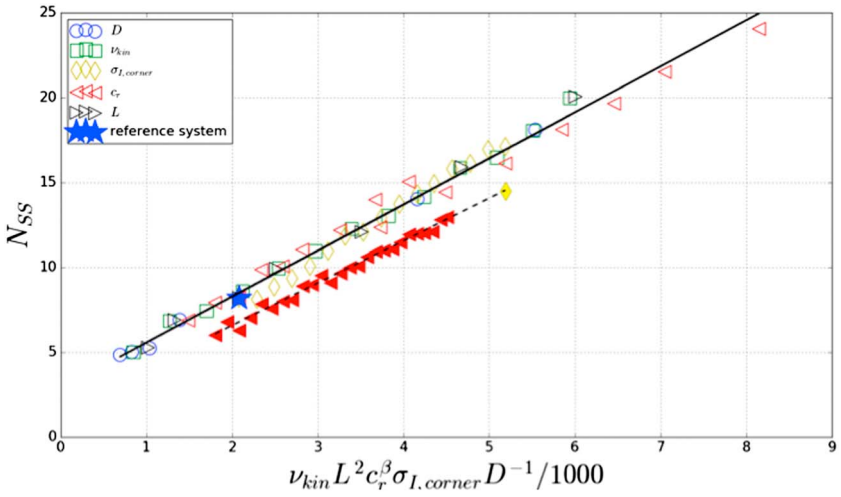

Figure 11. Variation of N_{SS} (ice bilayer difference between facet corner and center) with respect to variations in parameters of the model. The legend indicates parameters allowed to deviate from the reference system. Symbol sizes represent typical uncertainties of one standard deviation. The hollow symbols, star, and solid line correspond to the sinusoidal case. The solid symbols (except the star) and dashed line refer to the parabolic case.

Table 4. Parameter Variations Consistent With Steady States of the Continuum Model With Sinusoidal Inhomogeneity in the Vapor Field

	c_r (%)	D ($\mu m^2 \mu s^{-1}$)	L (μm)	v_{kin} ($\mu m\ s^{-1}$)	v_{kin} (bilayer μs^{-1})	$\sigma_{I,corner}$
Minimum	0.15	0.75×10^{-4}	17.5	20	0.07	0.20
Maximum	0.7	6×10^{-4}	42.5	140	0.47	0.50

3.5. Mechanism of Achieving Uniform Growth

In the one-dimensional system, the "problem" with maintaining uniform growth in the presence of excess water vapor over facet corners is that, absent some compensating mechanism, growth at corners will outpace growth at facet center. While the results presented here constitute compelling evidence for the existence of a such a mechanism (because steady state solutions exist), we have not probed the mechanism itself. One might imagine that excess vapor deposition at a facet corner would lead to thicker quasi-liquid at corners, which would then lead to enhanced diffusion, down-gradient, toward facet center. But this mechanism must be rejected for the model developed here (and, we believe, in reality) because surface diffusion is too slow compared to quasi-liquid/ice-like equilibration, which converts excess quasi-liquid to ice on a nanosecond time scale.

Instead, we seek a mechanism based on feedback. We propose a mechanism whereby diffusion at steady state influences growth through its impact on the efficiency with which the surface captures water vapor:

1. Terraces become more narrow at facet corners, compared to facet centers.
2. Terrace narrowing leads to enhanced surface diffusion, and (indirectly) to a reduction in the efficiency of vapor capture.

It follows from these steps that reduction in efficiency of vapor capture rate at corners compensates for the excess growth due to the imposed inhomogeneity in water vapor. We shall take step 1 as an empirical observation of the one-dimensional system: we observe that terraces become more narrow at facet corners compared to facet centers. It remains therefore to demonstrate step 2.

To do so, we focus on a single terrace, similar in form to those appearing in the right-hand side of Figure 9, but unaffected by diffusion. We do so by solving the zero-dimensional system for a given deposition rate, yielding $N_{tot}(t)$, $N_{QLL}(t)$, and $N_{ice}(t)$ over the course of a layer cycle, τ. These functions become initial conditions of a one-dimensional system having $D = 0$ and a terrace width w, spatially varying according to $N_{tot}(x)$, $N_{QLL}(x)$, and $N_{ice}(x)$, where $x = \left(\frac{w}{\tau}\right)t$. We then evaluate the change in the thickness of the ice/vapor interface, $\delta(N_{tot})$, that is due *directly* to the introduction of surface diffusion. This procedure is expressed as

$$\delta(N_{tot}) = \delta\left(D\nabla^2 N_{QLL}\right) = D\left(\frac{\tau}{w}\right)^2 \frac{\partial^2 N_{QLL}}{dt^2}. \tag{21}$$

Since N_{QLL} is the solution to the zero-dimensional problem (or equivalently, the one-dimensional problem with $D = 0$), this equation expresses the effect of diffusion as a perturbation. Now we recast this expression in terms of a scaled time, $t' = t/\tau$ so that $\frac{\partial^2(\ldots)}{dt^2} = \frac{\partial^2(\ldots)}{dt'^2}/\tau^2$, giving

$$\delta(N_{tot}) = D\left(\frac{1}{w}\right)^2 \frac{\partial^2 N_{QLL}}{\partial t'^2}. \tag{22}$$

The effect described by equation (22) is not directly useful for the purpose of computing changes in growth, because diffusion alone leads ultimately to only a redistribution of quasi-liquid. However, the *efficiency* with which the surface captures water vapor *does* depend on the distribution of quasi-liquid. To estimate this indirect effect, we compute the perturbation in the microscopic transition parameter, m (defined in equation (6)), resulting from the introduction of diffusion,

$$\delta(m) = \frac{D}{2N^*}\left(\frac{1}{w}\right)^2 \frac{\partial^2 N_{QLL}}{\partial t'^2}, \tag{23}$$

and hence the perturbation in the microscopic supersaturation, σ_m,

$$\delta(\sigma_m) = \frac{\partial \sigma_m}{\partial m}\delta(m) = -\sigma_o \frac{1+\sigma_I}{(1+m\sigma_o)^2}\delta(m), \tag{24}$$

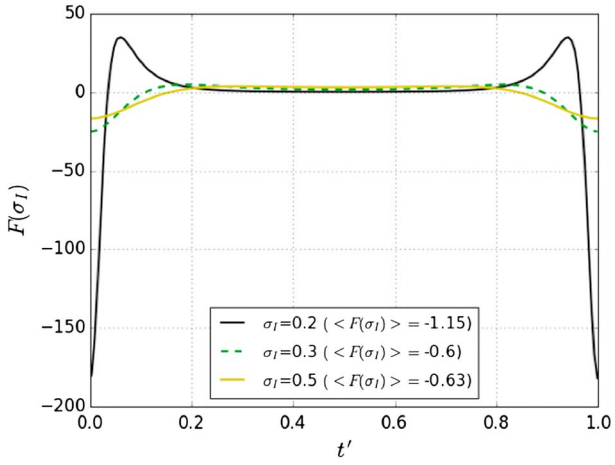

Figure 12. Indirect perturbation functions, $F(\sigma_I)$, equation (27), for the reference system and two other values of the supersaturation. The abscissa spans a single steady state terrace. Terrace averages are indicated in the legend.

where we have used equation (11) to evaluate the partial derivative. The resulting perturbation in the source term of equation (5a), which determines the growth due to the capture of water vapor, is therefore given by

$$\delta^{\text{ind}}(N_{\text{tot}}) = \delta(\sigma_m v_{\text{kin}}) = k\, F(\sigma_I)/w^2, \quad (25)$$

where we have collected constants as

$$k \equiv \frac{D\,\sigma_o v_{\text{kin}}}{2N^*}, \quad (26)$$

and defined an *indirect perturbation* function

$$F(\sigma_I) \equiv -\frac{1+\sigma_I}{(1+m\sigma_o)^2}\frac{\partial^2 N_{\text{QLL}}}{\partial t'^2}. \quad (27)$$

We display the indirect perturbation function over a range of supersaturations in Figure 12, as a function of the scaled time, t' (which may also be thought of as a distance parameter spanning a complete step/terrace/step interval). It is evident that the indirect effect of diffusion on vapor capture efficiency is greatest at terrace boundaries, i.e., close to steps, and most pronounced for small supersaturation. The legend of Figure 12 also shows mean values of $F(\sigma_I)$ over the same interval, from which it is evident that the indirect mechanism yields negative perturbations overall for all supersaturations. That is to say, our analysis predicts that diffusion causes an overall reduction in the steady state growth rate, via a modification in the distribution of quasi-liquid.

Figure 13 extends this analysis to other supersaturations. It shows that the indirect effect of diffusion on growth rate is to retard it for all supersaturations considered. When considered in the context of equation (25), $\delta^{\text{ind}}(N_{\text{tot}})$, we see that this effect is greater for narrower terraces (because of the w^2 in the denominator).

The foregoing perturbation analysis can be confirmed numerically by using the method of matched asymptotic expansions [*Verhulst*, 2005], in which a subdomain is defined as a single terrace of width w, bounded by a step on either side. Periodic boundary conditions are imposed across this subdomain. If we also impose a constant deposition rate across the subdomain, we have a series of identical terraces. Using the $D = 0$ solutions for a single terrace as described above ($N_{\text{tot}}(x)$, $N_{\text{QLL}}(x)$, and $N_{\text{ice}}(x)$) as initial conditions, we then solve the one-dimensional problem subject to different constraints, enabling us to evaluate the effects of varying diffusion coefficient and terrace width. We find that growth rates are consistent with the foregoing analysis, i.e., that systems with surface diffusion ($D > 0$) grow more slowly compared to systems without surface diffusion ($D = 0$) and that this slowdown is greater when terraces are narrow. Figure S2 in the supporting information shows a sample calculation.

In summary, we can understand the robustness of faceted growth in the presence of inhomogeneity in the water vapor field to be a consequence of the stabilizing effect of surface diffusion. Terrace centers have thicker quasi-liquid (hence are more similar to Microsurface II) compared to the steps that border them (which are more similar to Microsurface I); this means that terrace centers are less efficient at capturing water vapor compared to steps. But surface diffusion tends to redistribute quasi-liquid from regions where it is thick to where it is thin. Diffusion therefore increases capture efficiency at terrace centers and decreases capture efficiency at steps. The latter exceeds the former, resulting in a net slowdown in the vapor capture efficiency of the terrace overall. This "diffusive slowdown" is greater for narrower terraces, because narrower terraces have steeper spatial gradients of quasi-liquid thickness, all else equal. As mentioned above, steady state solutions *are* characterized by a narrowing of terraces at facet corners. Corners are therefore subject to greater diffusive slowdown, which compensates for the greater water vapor flux there, thereby enabling uniform faceted growth.

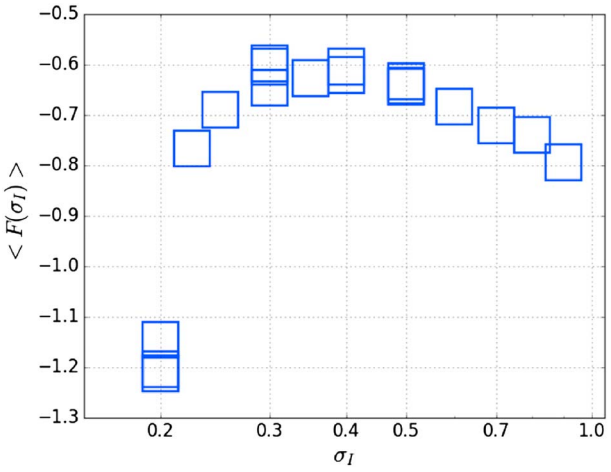

Figure 13. Mean values of indirect perturbation functions for the reference system, equation (27), over a range of imposed supersaturations.

4. Discussion

4.1. Properties of the Quasi-Liquid Layer

Our results point to the importance, in MD simulations, of paying attention to the way surfaces are prepared for study. The focus on annealed bilayers in prior MD studies (including work by the present authors) represents but one choice out of a continuum of possibilities that arise as ice growth proceeds. That choice, we argue, should be informed by the particular process of interest.

A separate issue concerns the functional dependence of the thickness of the QLL on N_{tot} chosen here (equation (3)), and the linear dependence of equilibrium vapor pressure on that thickness (equation (7)). These choices are not unique. A cursory investigation into the dynamics of the continuum model using other forms (but still satisfying the same periodicity and differentiability properties) revealed qualitatively similar behaviors to those presented here. However, a comprehensive exploration of this dependence has yet to be undertaken.

4.2. Why is Faceted Ice Growth Robust?

According to the Nelson-Baker (NB) mechanism [*Nelson and Baker*, 1996], uniform facet growth occurs because the ice surface evolves in such a way that steps grow closer together at facet centers. On the premise that ice formation at steps is more efficient than on terraces, reduced terrace widths at facet center compensate for lower deposition rates there.

Our results show that uniform growth does occur, which implies that the interior of the facet is indeed characterized by higher accommodation efficiency, and in this sense are consistent with the NB hypothesis. However, our results indicate that this enhanced efficiency is not associated with reduced terrace width at facet center, but rather the opposite: it relies fundamentally on a pattern of reduced terrace width at facet *corners*, away from facet center. The surfaces of these narrower terraces, in turn, are subject to more diffusive slowdown in growth rate via the dynamic linkage between quasi-liquid thickness and surface equilibrium vapor pressure over the course of a cycle of layer growth. Our model, moreover, shows that the development of this pattern is an emergent property of the system; i.e., solutions that characterize uniform growth can be described as a stable limit cycle or attractor.

4.3. Comparisons With Other Ice Growth Models.

In contrast to the Burton-Cabrera-Frank framework [*Cabrera and Burton*, 1949], the continuum model presented here is not valid in the low-surface-density regime, as it assumes complete coverage of the ice/vapor surface with quasi-liquid. It is, rather, relevant in the temperature regime above this threshold, which, based on prior work, occurs on the prismatic facet at around − 35℃ [*Gladich et al.*, 2011, 2015]. In other words, the continuum model represents a high-temperature complement to BCF theory.

In contrast with three-dimensional cellular automata theories of ice crystal growth [*Gravner and Griffeath*, 2009], the model presented here is only one-dimensional. The model shares with automata theory the notion that critical ingredients include a proper accounting of exchange between the ice and vapor phases, and the exchange between quasi-liquid and ice-like molecules. The model complements these theories in certain ways as well: its relationship to microscopic surface processes is more transparent, and it replicates faceted growth, which has so far vexed three-dimensional cellular automata theories [*Kelly and Boyer*, 2014].

In general terms, our results support the notion of structure-dependent attachment kinetics as governed by microscopic structure and dynamics [see *Libbrecht*, 2003a, 2003b, 2008]. In particular, our results affirm that

key microscopic characteristics are the diffusivity of quasi-liquid and cyclical variations in the thickness and equilibrium vapor pressure (a proxy for chemical potential) of quasi-liquid that occur as the surface adds bilayers during growth.

4.4. Limitations

The chief physical shortcoming of the model lies in its inability to grow ice when the surface supersaturation is smaller than the critical supersaturation. This emerges directly from our interpretation of the MD-derived microsurfaces as unique states with definite properties. However, it is clear from the MD results presented here that some quantities are inherently noisy. Figure 4, for example, indicates fluctuations in quasi-liquid thickness on the order of 10% on a time scale of tens of nanoseconds, while Table 1 indicates fluctuations in microsurface vapor pressure on a similar time scale. This means that some parameters of the continuum model, e.g., the critical supersaturation, are subject to fluctuations that cannot be adequately represented as simple averages. More broadly, our MD-derived results are based on a single model, NE6 water, whereas it is known that different models express different structural properties of the ice/vapor interface. These uncertainties are mitigated, however, by the observation that our qualitative results do not depend strongly on the precise choice of key properties of the ice/vapor interface: we obtain steady state solutions for a wide range of diffusion coefficients and critical supersaturations. A more sophisticated, probabilistic incorporation of MD simulation results in the model could overcome such limitations, although this remains to be demonstrated. A second limitation is numerical rather than physical and concerns the difficulty in disentangling instabilities that arise for numerical reasons, from those that reflect physical sources of instability. While the integration algorithm used here (described in section 3.2) is straightforward and easy to implement, others are more stable and efficient and are worth exploring. Other limitations include that macroscopic steps cannot form in our simulations given the initial (flat) configuration, and that as a one-dimensional model, it cannot reproduce intrinsically two-dimensional spatial instabilities [*Bales and Zangwill*, 1990; *Krug*, 2005]. These extensions will be addressed in future work in this area.

5. Conclusions

We have presented a continuum model for ice growth consisting of partial differential equations, in which grid points represent microsurfaces that undergo sub-grid-scale dynamic partitioning of the ice/vapor interface into ice and quasi-liquid components. The model shares many features in common with classical BCF theory but differs in that it is relevant in the high-surface-density admolecule regime characteristic of warmer ($T > -35$ ℃) ice. Off-line MD simulations supply key atomistic insight into these microsurfaces, namely, that the quasi-liquid exhibits periodic variability in thickness and equilibrium vapor pressure as a function of total surface thickness. Numerical solutions of the continuum model show that these microsurfaces play a decisive role in the emergence and robustness of uniform crystal growth and lead to the interpretation of uniform crystal growth as a stable limit cycle of the underlying nonlinear dynamics. A mechanism is proposed in which a narrowing of terrace widths at facet corners plays a key role in making uniform crystal growth possible.

Acknowledgments

S.N. was supported by the NSF grant award CHE-1306366 for this work and acknowledges support from a University of Puget Sound Lantz Senior Sabbatical Fellowship and the Fulbright Scholar program. J.A. and K.R. acknowledge support from the University of Puget Sound. P.M.R. received support from the Consejo Nacional de Ciencia y Tecnologia CONICYT- Anillos, Preis ACT 1410 and FONDECYT Regular 1161460. We thank Marcelo Carignano, Jon Nelson, and Gregory Henselman for insightful comments and suggestions; Aedin Wright for assistance in computation; and three anonymous reviewers, whose comments greatly improved the organization and content of the manuscript. Computer codes implementing the continuum model are available at https://github.com/upschemistry/ice-continuum. There are no data sharing issues since all numerical information is provided in figures and tables in this paper and in a supporting information file; the latter contains two figures and two videos. Any additional data may be obtained from S.N. (e-mail: nesh@pugetsound.edu).

References

Abascal, J. L. F., and C. Vega (2005), A general purpose model for the condensed phases of water: TIP4P/2005, *J. Chem. Phys.*, *123*, 234,505.

Abascal, J. L. F., R. G. Fernandez, C. Vega, and M. A. Carignano (2006), The melting temperature of the six site potential model of water, *J. Chem. Phys.*, *125*(16), 166,101–2, doi:10.1063/1.2360276.

Abraham, M. J., T. Murtola, R. Schulz, S. Páll, J. C. Smith, B. Hess, and E. Lindahl (2015), GROMACS: High performance molecular simulations through multi-level parallelism from laptops to supercomputers, *SoftwareX*, *1*, 19–25.

Bailey, M., and J. Hallett (2004), Growth Rates and Habits of Ice Crystals between −20° and −70°C, *J. Atmospheric Sci.*, *61*(5), 514–544.

Bailey, M. P., and J. Hallett (2009), A comprehensive habit diagram for atmospheric ice crystals: Confirmation from the laboratory, AIRS II, and other field studies, *J. Atmospheric Sci.*, *66*(9), 2888–2899, doi:10.1175/2009JAS2883.1.

Bales, G. S., and A. Zangwill (1990), Morphological instability of a terrace edge during step-flow growth, *Phys. Rev. B*, *41*(9), 5500–5508, doi:10.1103/PhysRevB.41.5500.

Baran, A. J. (2009), A review of the light scattering properties of cirrus, *J. Quant. Spectrosc. Radiat. Transf.*, *110*(14–16), 1239–1260.

Baran, A. J. (2015), On the relationship between the scattering phase function of cirrus and the atmospheric state, *Atmospheric Chem. Phys.*, *15*, 1105–1127, doi:10.5194/acp-15-1105-2015.

Bartels-Rausch, T., et al. (2012), Ice structures, patterns, and processes: A view across the icefields, *Rev. Mod. Phys.*, *84*(2), 885–944, doi:10.1103/RevModPhys.84.885.

Bartels-Rausch, T., et al. (2014), A review of air–ice chemical and physical interactions (AICI): liquids, quasi-liquids, and solids in snow, *Atmospheric Chem. Phys.*, *14*(3), 1587–1633, doi:10.5194/acp-14-1587-2014.

Batista, E. R., P. Ayotte, A. Bilic, B. D. Kay, and H. Jonsson (2005), What determines the sticking probability of water molecules on ice?, *Phys. Rev. Lett.*, *95*(22), 223,201–4, doi:10.1103/PhysRevLett.95.223201.
Berendsen, H. J., J. van Postma, W. F. van Gunsteren, A. DiNola, and J. R. Haak (1984), Molecular dynamics with coupling to an external bath, *J. Chem. Phys.*, *81*(8), 3684–3690.
Bevington, P. R., and D. K. Robinson (1993), *Data Reduction and Error Analysis for the Physical Sciences*, 2nd ed., McGraw-Hill, New York.
Buch, V., P. Sandler, and J. Sadlej (1998), Simulations of H2O solid, liquid, and clusters, with an emphasis on ferroelectric ordering transition in hexagonal ice, *J. Phys. Chem. B*, *102*(44), 8641–8653.
Burton, W. K., and N. Cabrera (1949), Crystal growth and surface structure. Part I, *Discuss. Faraday Soc.*, *5*(0), 33–39.
Burton, W. K., N. Cabrera, and F. C. Frank (1951), The growth of crystals and the equilibrium structure of their surfaces, *Philos. Trans. R. Soc. Lond. Ser. Math. Phys. Sci.*, *243*, 299–358.
Bussi, G., D. Donadio, and M. Parrinello (2007), Canonical sampling through velocity rescaling, *J. Chem. Phys.*, *126*(1), 14,101, doi:10.1063/1.2408420.
Cabrera, N., and W. K. Burton (1949), Crystal growth and surface structure. Part II, *Discuss. Faraday Soc.*, *5*(0), 40–48.
Curto, C., and V. Itskov (2008), Cell groups reveal structure of stimulus space, *PLoS Comput. Biol.*, *4*(10), e1000205.
Errington, J. R., and P. G. Debenedetti (2001), Relationship between structural order and the anomalies of liquid water, *Nature*, *409*(6818), 318–321, doi:10.1038/35053024.
Essmann, U., L. Perera, M. L. Berkowitz, T. Darden, H. Lee, and L. G. Pedersen (1995), A smooth particle mesh Ewald method, *J. Chem. Phys.*, *103*(19), 8577–8593, doi:10.1063/1.470117.
Fu, Q., and K. N. Liou (2008), Parameterization of the radiative properties of cirrus clouds, *J. Atmospheric Sci.*, *50*, 13.
Girardet, C., and C. Toubin (2001), Molecular atmospheric pollutant adsorption on ice: A theoretical survey, *Surf. Sci. Rep.*, *44*(7–8), 159–238, doi:10.1016/S0167-5729(01)00016-4.
Gladich, I., and M. Roeselová (2012), Comparison of selected polarizable and nonpolarizable water models in molecular dynamics simulations of ice Ih, *Phys. Chem. Chem. Phys.*, *14*(32), 11,371–11,385, doi:10.1039/C2CP41497J.
Gladich, I., W. Pfalzgraff, O. Maršálek, P. Jungwirth, M. Roeselová, and S. Neshyba (2011), Arrhenius analysis of anisotropic surface self-diffusion on the prismatic facet of ice, *Phys. Chem. Chem. Phys.*, *13*(44), 19,960–19,969.
Gladich, I., A. Oswald, N. Bowens, S. Naatz, P. Rowe, M. Roeselova, and S. Neshyba (2015), Mechanism of anisotropic surface self-diffusivity at the prismatic ice–vapor interface, *Phys. Chem. Chem. Phys.*, *17*(35), 22,947–22,958.
Gravner, J., and D. Griffeath (2009), Modeling snow-crystal growth: A three-dimensional mesoscopic approach, *Phys. Rev. E*, *79*(1), 11,601-1-11,601-18.
Guignard, A., C. J. Stubenrauch, A. J. Baran, and R. Armante (2012), Bulk microphysical properties of semi-transparent cirrus from AIRS: A six year global climatology and statistical analysis in synergy with geometrical profiling data from CloudSat-CALIPSO, *Atmospheric Chem. Phys.*, *12*(1), 503–525.
Hallett, J. (1961), The growth of ice crystals on freshly cleaved covellite surfaces, *Philos. Mag.*, *6*(69), 1073–1087, doi:10.1080/14786436108239669.
Hindmarsh, A. C. (1983), in ODEPACK: A Systematized Collection of ODE Solvers, in *IMACS Trans. Sci. Comput.*, vol. 1 edited by R. S. Stepleman et al., pp. 55–64, North-Holland, Amsterdam.
Hobbs, P. V. (2010), *Ice Physics*, Oxford Univ. Press, Oxford.
Hobbs, P. V., and W. D. Scott (1965a), A theoretical study of the variation of ice crystal habits with temperature, *J. Geophys. Res.*, *70*(20), 5025–5034, doi:10.1029/JZ070i020p05025.
Hobbs, P. V., and W. D. Scott (1965b), Step-growth on single crystals of ice, *Philos. Mag.*, *11*(113), 1083–1086.
Hockney, R. W., S. P. Goel, and J. W. Eastwood (1974), Quiet high-resolution computer models of a plasma, *J. Comput. Phys.*, *14*(2), 148–158, doi:10.1016/0021-9991(74)90010-2.
Kelly, J. G., and E. C. Boyer (2014), Physical improvements to a mesoscopic cellular automaton model for three-dimensional snow crystal growth, *Cryst. Growth Des.*, *14*(3), 1392–1405, doi:10.1021/cg401862u.
Kong, X. (2014), Molecular investigations of atmospherically relevant interface processes: Ice formation and water accommodation on ice and organic surfaces, Thesis for the degree of Doctor of Philosophy in Natural Science, Univ. of Gothenburg.
Kong, X., P. Papagiannakopoulos, E. S. Thomson, N. Marković, and J. B. C. Pettersson (2014), Water accommodation and desorption kinetics on ice, *J. Phys. Chem. A*, *118*(22), 3973–3979, doi:10.1021/jp503504e.
Krug, J. (2005), Introduction to step dynamics and step instabilities, in *Multiscale Modeling in Epitaxial Growth*, vol. 149, edited by A. Voigt, pp. 69–95, Birkhäuser Basel, Switzerland.
Libbrecht, K. G. (2003a), Explaining the formation of thin ice crystal plates with structure-dependent attachment kinetics, *J. Cryst. Growth*, *258*(1), 168–175.
Libbrecht, K. G. (2003b), Growth rates of the principal facets of ice between −10°C and −40°C, *J. Cryst. Growth*, *247*(3), 530–540.
Libbrecht, K. G. (2005), The physics of snow crystals, *Rep. Prog. Phys.*, *68*, 855.
Libbrecht, K. G. (2008), Crystal growth in the presence of surface melting and impurities: An explanation of snow crystal growth morphologies Arxiv Prepr. ArXiv08100689.
Libbrecht, K. G., and M. E. Rickerby (2013), Measurements of surface attachment kinetics for faceted ice crystal growth, *J. Cryst. Growth*, *377*, 1–8, doi:10.1016/j.jcrysgro.2013.04.037.
Lynch, D. K. (2002), *Cirrus*, Oxford Univ. Press, New York.
Magee, N., A. M. Moyle, and D. Lamb (2006), Experimental determination of the deposition coefficient of small cirrus-like ice crystals near −50°C, *Geophys. Res. Lett.*, *33*, L17813, doi:10.1029/2006GL026665.
Miyamoto, S., and P. A. Kollman (1992), Settle: An analytical version of the SHAKE and RATTLE algorithm for rigid water models, *J. Comput. Chem.*, *13*(8), 952–962, doi:10.1002/jcc.540130805.
Muchová, E., I. Gladich, S. Picaud, P. N. Hoang, and M. Roeselová (2011), The ice-vapor interface and the melting point of ice Ih for the polarizable POL3 water model, *J. Phys. Chem. A*, *115*(23), 5973–5982.
Myers-Beaghton, A. K., and D. D. Vvedensky (1991), Generalized Burton-Cabrera-Frank theory for growth and equilibration on stepped surfaces, *Phys. Rev. A*, *44*(4), 2457–2468, doi:10.1103/PhysRevA.44.2457.
Nada, H., and J. P. J. M. van der Eerden (2003), An intermolecular potential model for the simulation of ice and water near the melting point: A six-site model of HO, *J. Chem. Phys.*, *118*, 7401–7413.
Nelson, J. T., and M. B. Baker (1996), New theoretical framework for studies of vapor growth and sublimation of small ice crystals in the atmosphere, *J. Geophys. Res.- Sect.*, *101*, 7033–7047.

Neshyba, S., E. Nugent, M. Roeselová, and P. Jungwirth (2009), Molecular dynamics study of ice-vapor interactions via the quasi-liquid layer, *J. Phys. Chem. C*, *113*(11), 4597–4604, doi:10.1021/jp810589a.
Nicolis, G., et at. (1977), *Self-Organization in Nonequilibrium Systems*, Wiley, New York.
Oliphant, T. E. (2006), *A Guide to NumPy*, Trelgol, USA.
Patrone, P. (2013), Modeling of interfaces: Applications in surface and polymer physics PhD. Dissertation, Univ. of Maryland, College Park, Md.
Patrone, P. N., T. L. Einstein, and D. Margetis (2014), From atoms to steps: The microscopic origins of crystal evolution, *Surf. Sci.*, *625*, 37–43.
Petrenko, V. F., and R. W. Whitworth (1999), *Physics of Ice*, Oxford, University Press.
Pfalzgraff, W., S. Neshyba, and M. Roeselova (2011), Comparative molecular dynamics study of vapor-exposed basal, prismatic, and pyramidal surfaces of ice, *J. Phys. Chem. A*, *115*, 6184–6193.
Pi, H. L., J. L. Aragones, C. Vega, E. G. Noya, J. L. F. Abascal, M. A. Gonzalez, and C. McBride (2009), Anomalies in water as obtained from computer simulations of the TIP4P/2005 model: Density maxima, and density, isothermal compressibility and heat capacity minima, *Mol. Phys.*, *107*(4–6), 365–374, doi:10.1080/00268970902784926.
Pratte, P., H. van den Bergh, and M. J. Rossi (2006), The kinetics of H2O vapor condensation and evaporation on different types of ice in the range 130–210 K, *J. Phys. Chem. A*, *110*(9), 3042–3058, doi:10.1021/jp053974s.
Sadtchenko, V., and G. E. Ewing (2003), A new approach to the study of interfacial melting of ice: infrared spectroscopy, *Can. J. Phys.*, *81 1*(2), 333–341.
Sadtchenko, V., M. Brindza, M. Chonde, B. Palmore, and R. Eom (2004), The vaporization rate of ice at temperatures near its melting point, *J. Chem. Phys.*, *121*(23), 11,980–11,992, doi:10.1063/1.1817820.
Saito, Y. (1996), *Statistical Physics of Crystal Growth*, World Scientific, N. J.
Sazaki, G., S. Zepeda, S. Nakatsubo, E. Yokoyama, and Y. Furukawa (2010), Elementary steps at the surface of ice crystals visualized by advanced optical microscopy, *Proc. Natl. Acad. Sci.*, *107*(46), 19,702–19,707.
Schnaiter, M., et al. (2016), Cloud chamber experiments on the origin of ice crystal complexity in cirrus clouds, *Atmospheric Chem. Phys.*, *16*(8), 5091–5110, doi:10.5194/acp-16-5091-2016.
Shultz, M. J., P. J. Bisson, and A. Brumberg (2014), Best face forward: Crystal-face competition at the ice–water interface, *J. Phys. Chem. B*, *118*(28), 7972–7980, doi:10.1021/jp500956w.
Stephens, G., S. Tsay, P. W. Stackhouse, and P. J. Flatau (1990), The relevance of the microphysical and radiative properties of cirrus clouds to climate and climatic feedback, *J. Atmospheric Sci.*, *47*(14), 1742–1753.
Vega, C., J. L. F. Abascal, and P. G. Debenedetti (2011), Physics and chemistry of water and ice, *Phys. Chem. Chem. Phys.*, *13*(44), 19,660–19,662.
Verhulst, F. (2005), *Methods and Applications of Singular Perturbations: Boundary Layers and Multiple Timescale Dynamics*, Springer Science & Business Media, N. J.
Yang, P., and K. N. Liou (1998), Single-scattering properties of complex ice crystals in terrestrial atmosphere, *Beitrage Zur Phys. Atmosphare-Contrib. Atmospheric Phys.*, *71*(2), 223–248.
Ye, Y.-Q., and C. Y. Lo (1986), *Theory of Limit Cycles*, Am. Mathematical Soc, Providence, R. I.